Moving Wall Effects in Unsteady Flow

L. E. Ericsson
Lockheed Missiles & Space Company, Inc., Sunnyvale, California

Nomenclature

c = cross-sectional chord length, $c = D$ for a circular cylinder
D = cylinder diameter
d^1 = sectional drag: coefficient $c_d = d^1/(\rho_\infty U_\infty^2/2)$
f = frequency of oscillating body
f_o = natural frequency of oscillating body
f_p = frequency of pressure oscillation
f_v = frequency of Kármán vortex shedding
f_{vo} = f_v for stationary cylinder
l = body length
ℓ = cross-sectional lift: coefficient $c_\ell = \ell/(\rho_\infty U_\infty^2/2)c$
m_p = cross-sectional pitching moment: coefficient $c_m = m_p/(\rho_\infty U_\infty^2/2)c^2$
P = static pressure: coefficient $C_p = (P - P_\infty)/(\rho_\infty U_\infty^2/2)$
p = rotation or spin rate
Re = Reynolds number, usually $Re = Re_c = U_\infty c/\nu_\infty$
r = cylinder radius, $r = D/2$
S = reference area, $S = \pi D^2/4$
t = time
U = freestream horizontal velocity
U_W = wall velocity
x = chordwise or axial distance from leading edge or apex
Y = sideforce: coefficient $C_Y = Y/(\rho_\infty U_\infty^2/2)S$; $c_y = \partial C_y/\partial\xi$
z = translatory coordinate
$\dot{z}$ = $\partial z/\partial t$, $\ddot{\psi} = \partial^2\psi/\partial t^2$, $c_{\ell\alpha} = \partial c_\ell/\partial\alpha$
α = angle of attack
α_o = trim angle of attack
$\bar{\alpha}$ = equivalent amplitude, $\bar{\alpha} = |\dot{z}|/U_\infty$
β^* = local side slip angle, $\approx U_W/U_\infty$
Δ = increment or amplitude
ζ_o = mechanical damping, fraction of critical
θ = perturbation in pitch or torsion
θ^* = equivalent pitch perturbation, Eq. (1)
ν = kinematic viscosity
ξ = dimensionless coordinate, $\xi = x/c$
ρ = fluid density
σ = total flow inclination
ϕ = phase angle
φ = peripheral angle, $\varphi = 0$ at the stagnation point
ψ = coning angle
$\Omega,\bar{\Omega}$ = flat-spin rate, $\Omega = \partial\psi/\partial t$ for $\alpha = 90$ deg, $\bar{\Omega} = \Omega l/U_\infty$
$\omega,\bar{\omega}$ = oscillation frequency, $\omega = 2\pi f$, $\bar{\omega} = \omega c/U_\infty$

Subscripts

AV = asymmetric vortices
F = forebody
FS = flat spin
max = maximum
min = minimum
N = nose tip
s = separation
sp = separation point
SV = symmetric vortices
UV = unsteady vortices
v = vortex
vg = vortex growth
W = wall
WR = wing rock
1,2 = numbering subscripts
∞ = freestream conditions

Superscripts

$(-)$ = integrated time-average value, e.g., $\bar{c}_\ell(t)$

Introduction

THE classic moving wall effect generating so-called Magnus lift[1] is well recognized (for example, see Swanson's review[2]). In contrast, the fact that very similar moving wall effects are present for other types of body motion and for a variety of body geometries has largely been ignored. It is the purpose of this paper to remove this ignorance by showing numerous examples from both two-dimensional and three-dimensional flow; in short, the dynamic omnipresence of moving wall effects will be demonstrated.

Moving Wall Effects

Moving wall effect, as used in the present paper, refers to the unsteady boundary condition at the body surface between flow stagnation and separation points. A rotating circular cylinder presents a well-known case of moving wall effects in stationary flow, and the experimental results presented by Swanson[2] will be used as the starting point and reference when discussing other types of moving wall effects. The wall jet-like effect of the moving wall is illustrated in Fig. 1 (for the case $U_W/U_\infty = 1$). On the top side, downstream moving wall effects fill out the boundary-layer velocity profile, thereby delaying flow separation, whereas on the bottom half upstream moving wall effects

L. E. Ericsson is a Senior Consulting Engineer in the Engineering Technology Organization of Lockheed Missiles and Space Corporation, Inc., Sunnyvale, California, where he acts as a consultant to the Satellite and Missile Systems Divisions on problems associated with aeroelasticity and vehicle dynamics. Before joining Lockheed Aircraft Corporation in 1956, and LMSC in 1959, he was with the Aeronautical Research Institute of Sweden and the Swedish Aircraft Company, SAAB. Dr. Ericsson received his M.S. degree from the Royal Institute of Technology (KTH), Stockholm, in 1949, and his Ph.D. in 1972. He is a Fellow of the AIAA and is a member of the American Helicopter Society. Dr. Ericsson has published over 100 papers in his related fields.

Presented as Paper 87-0241 at the AIAA 25th Aerospace Sciences Meeting, Reno, NV, Jan. 12–15, 1987; received Dec. 11, 1986; revision received Jan. 9, 1988.

promote separation. The upstream moving wall effects are by far the strongest, as is demonstrated by comparing the Magnus lift for laminar (subcritical, Fig. 2) and turbulent (supercritical, Fig. 3) flow conditions.[2,3] (The nomenclature refers to the initial boundary-layer conditions existing at $p = 0$). In the laminar case, the Magnus lift is generated mainly by the downstream moving wall effect on the top side, moving the separation from the subcritical towards the supercritical position (Fig. 2). On the bottom side, the separation is already of the subcritical type at $p = 0$, and the upstream moving wall effect does not have much leverage for its separation-promoting action. In the turbulent case (Fig. 3), however, the situation is reversed. The main effect is that of the upstream moving wall on the bottom side, promoting separation, moving it from the supercritical towards the subcritical position. The difference in Magnus lift slopes, the turbulent one being three times as large as the laminar one, reflects the fact that the adverse (upstream) moving wall effect is the largest, as would be expected.

These moving wall effects on laminar and turbulent flow separation are rather straightforward and explain the positive Magnus lift slopes. The negative slopes, the so-called Magnus lift reversals, are caused by the moving wall effect on boundary-layer transition. In the laminar case (Fig. 2), when $p < p_{crit}$, the upstream moving wall effect on the bottom side causes transition to occur before separation, changing it from the subcritical toward the supercritical type. This effect completely overpowers the regular moving wall effects and causes a more or less discontinuous loss of lift (Fig. 2). In the turbulent case (Fig. 3), it is the downstream moving wall effect on the top side that delays transition, causing it to move downstream of the separation point, thereby changing the separation from the supercritical towards the subcritical type. This also generates a more or less discontinuous loss of lift.

Critical Reynolds Number

In both cases of Magnus lift just discussed, the changes were towards—but not all the way to—the subcritical or supercritical types, the full change being restricted by the "regular" moving wall effects. However, at critical flow conditions these restrictions are no longer present. As a result, the lift loss is larger and is generated immediately when p changes from $p = 0$ to $p \neq 0$ (Fig. 4). In the critical Reynolds number region the flow separation is dominated by the presence of a laminar separation bubble. The laminar flow separation develops near the lateral meridian ($\varphi = 90$ deg) and is followed by transition in the lifted shear layer, which causes flow reattachment. The reattaching "freshly" turbulent boundary layer is able to withstand the adverse pressure gradient until $\varphi \approx 140$ deg before separation occurs. This is far aft of the separation location for a fully turbulent boundary layer $\varphi \approx 100$ deg, resulting in a "drag bucket" for the critical Reynolds number region[4] (Fig. 5).

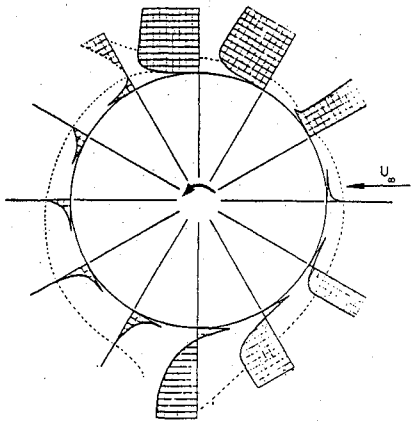

Fig. 1 Computed boundary layer flow profiles on a rotating cylinder with $U_W/U_\infty = 1$.[2]

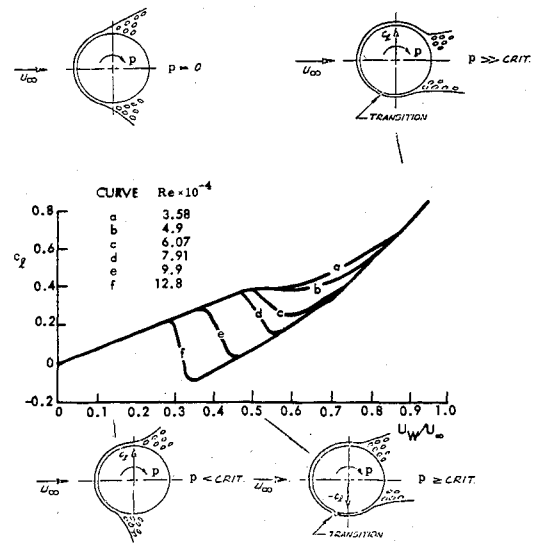

Fig. 2 Moving wall effects on a rotating cylinder with laminar flow conditions.

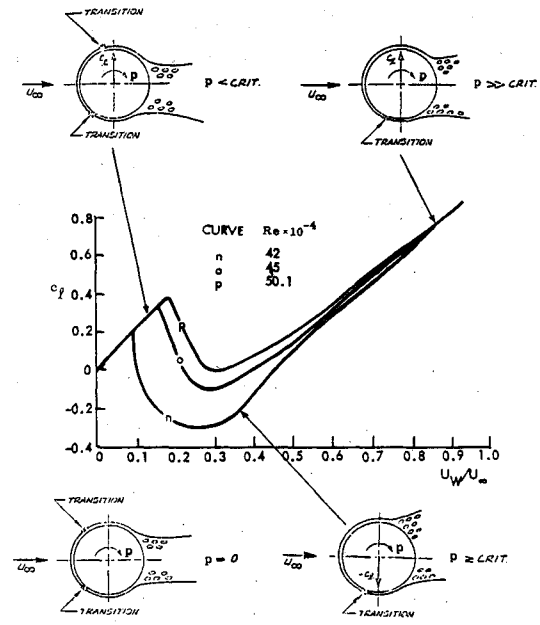

Fig. 3 Measured Magnus lift on a rotating cylinder with turbulent initial flow conditions.

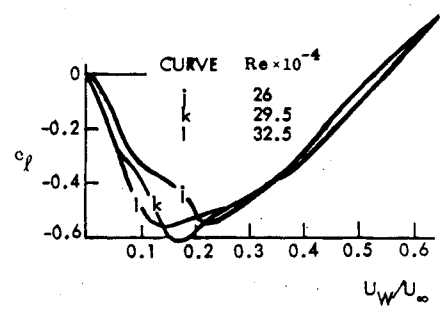

Fig. 4 Measured Magnus lift on a rotating circular cylinder at critical flow conditions.[2]

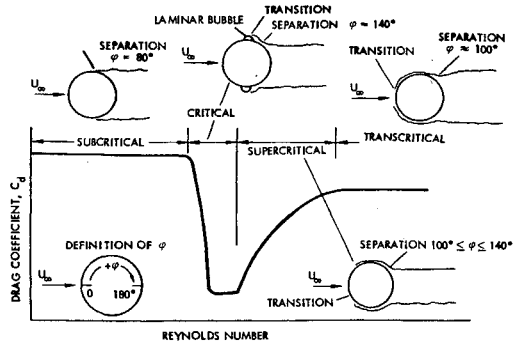

Fig. 5 Flow regions for a circular cylinder.[4]

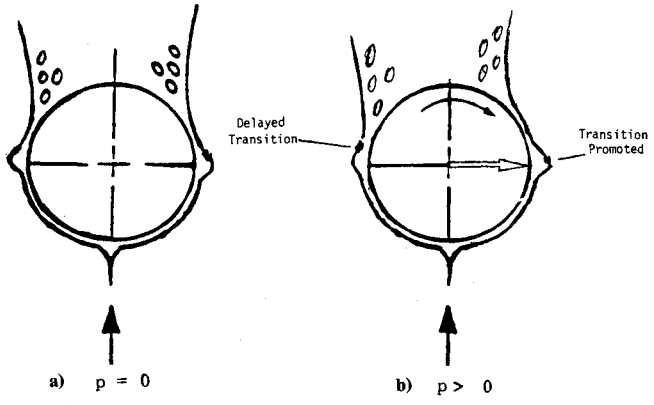

Fig. 6 Moving wall effects on rotating cylinder at critical flow conditions.

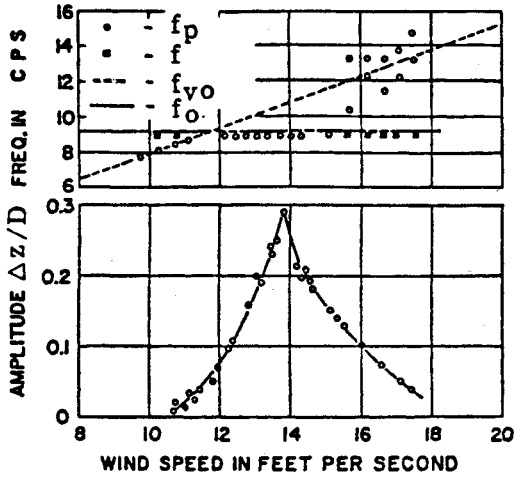

Fig. 7 Lateral response of a circular cylinder to Kármán vortex shedding at subcritical flow conditions.[5]

When the Reynolds number is increased, transition moves forward in the raised shear layer forming the bubble. This generates a fuller turbulent-flow profile in the reattaching shear layer, resulting in a delay of the final, turbulent-flow separation. This amplification of the beneficial effects of increasing Reynolds number will continue until transition reaches its most forward location on the top of the bubble. Transition will remain there until the Reynolds number has been increased enough to overcome the transition delay caused by local accelerated flow effects. The minimum drag plateau in Fig. 5 would result from such momentary arrest of the forward transition movement with increasing Reynolds number. When transition is increased further, transition jumps forward of the bubble,

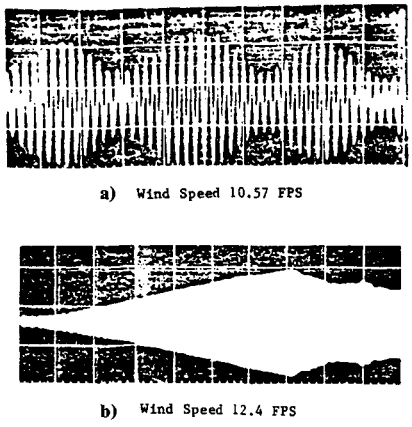

Fig. 8 Response amplitude characteristics below and above resonance.[5]

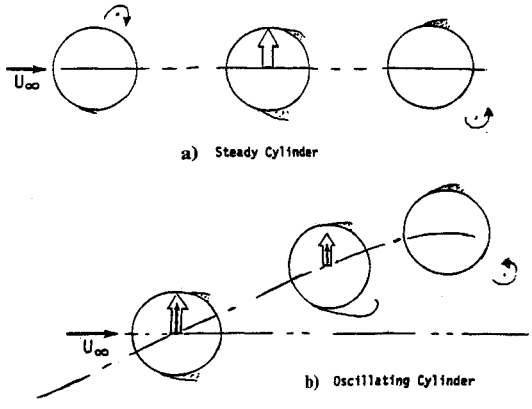

Fig. 9 Unsteady flow separation on steady and oscillating circular cylinder at $f < f_{vo}$.[10]

wiping it out. The resulting supercritical type separation increases with increasing Reynolds number resulting in increased drag (Fig. 5).

The first part of the critical flow region in Fig. 5, with its sharp drop of c_d with increasing Reynolds number until the minimum drag plateau is reached, corresponds to the Reynolds number region in Fig. 4, giving the negative Magnus lift slope. In the case of a rotating circular cross section (Fig. 6), the upstream moving wall effects causes a forward movement of transition in the lifted shear layer, forming the laminar separation bubble. As is sketched in Fig. 6b, the resulting separation delay produces increased suction, generating negative lift. A similar contribution to the negative Magnus lift in Fig. 4 is generated by the transition delay caused by the downstream moving wall effects on the opposite side. This promotes flow separation and causes a loss of suction.

The results shown in Figs. 1–6 are going to be used in what follows to explain the observed moving wall effects for other body motions and other body geometries, both in two-dimensional and three-dimensional flow.

Two-Dimensional Flow

Changing the motion of the circular cylinder from steady-state rotation to oscillatory translation, one obtains results such as those[5,6] presented in Fig. 7. The figure shows that the cylinder response at resonance, $U_\infty \approx 11.5$ fps, is only a fraction of the maximum response at $U_\infty \approx 13.5$ fps. Figure 8 shows that the response below the resonant wind velocity, at $U_\infty = 10.57$ fps, is of the forced oscillation type expected near resonant conditions, whereas the response at higher velocity, $U_\infty = 12.4$ fps, shows the build-up to a limit cycle amplitude characteristic of an oscillatory system subject to nonlinear negative damping.[7] The latter type of cylinder response, the so-

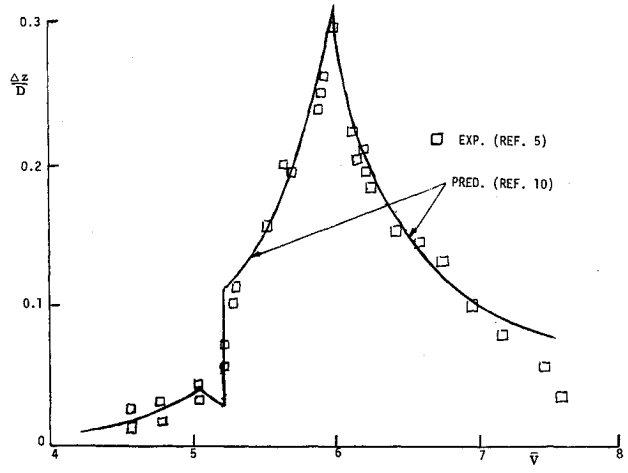

Fig. 10 Predicted and measured subcritical response to Kármán vortex shedding.[10]

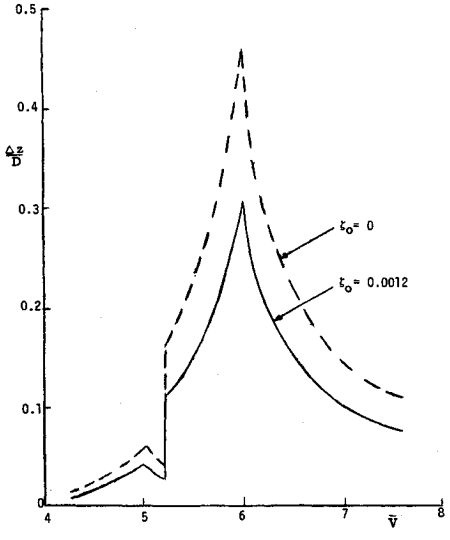

Fig. 11 Effect of mechanical damping on response amplitude.[10]

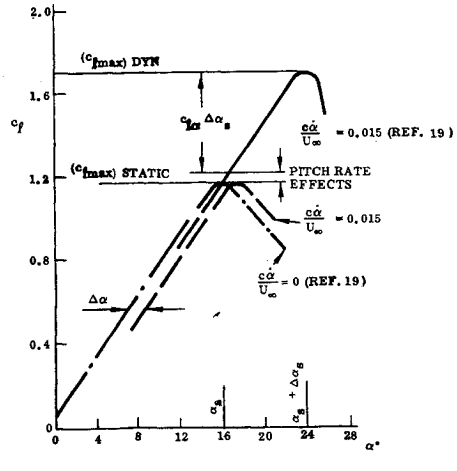

Fig. 12 Composition of α-ramp overshoot of static $c_{\ell\,max}$.[18]

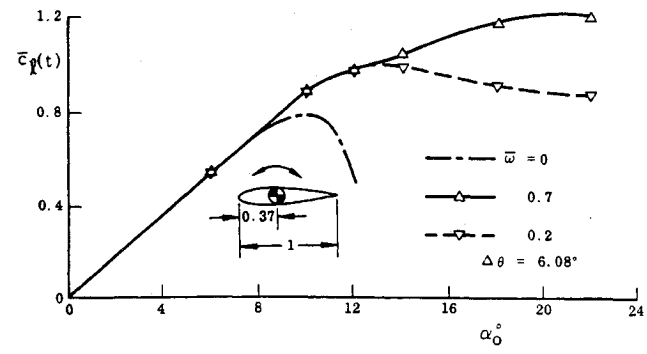

Fig. 13 Time-average lift for a thin airfoil describing oscillation in pitch at $Re = 10^6$.[21]

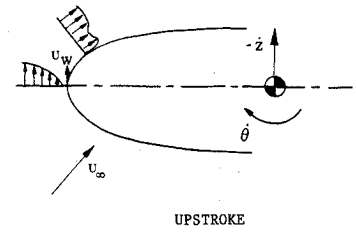

Fig. 14 "Leading edge jet" effect.[22]

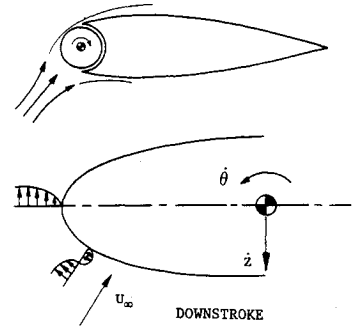

called lock-on or synchronization, occurs when a certain threshold value, $\Delta z/D \approx 0.02$, is exceeded.[8,9]

When the threshold amplitude is exceeded and vortex lock-on occurs, the response is a result of the coupling between body motion and the oscillatory flow separation associated with the Kármán vortex shedding.[3,9,10] The self-excited response observed for galloping cables,[11] for example, is, as a rule, occurring without such coupling effects. As a matter of fact, coupling with the Kármán vortex shedding can inhibit the galloping.[12] However, the maximum response of the circular cylinder, shown in Fig. 1, can occur only through a strong coupling between the Kármán vortex shedding and the body motion. The flow concept used by the present author in Refs. 3, 9, and 10 is similar to the "oscillatory Magnus" effect suggested by others in Refs. 13 and 14. The difference is that the moving wall effect on flow separation is considered to be the dominant flow phenomenon in one case,[3,9,10] whereas in the other some form of momentum transfer to the inviscid ambient fluid through feedback from the oscillating wake is the proposed flow mechanism.[13,14]

There is a good deal of similarity between the moving wall effect on dynamic stall[15] and the corresponding effect on a rotating[2] or translating[5,6] circular cylinder, as was pointed out in Refs. 3, 9, and 10 and is illustrated in Fig. 9. The open vector denotes the lift and the solid vector the translatory velocity ($\dot{z}$). When the cylinder oscillates at a frequency below that of the Kármán vortex shedding frequency for a steady (nonoscillating) cylinder, the flow separation delay due to the moving wall effect will drive the motion, i.e., negative aerodynamic damping is generated. For the rotating cylinder in Figs. 1–6 the moving

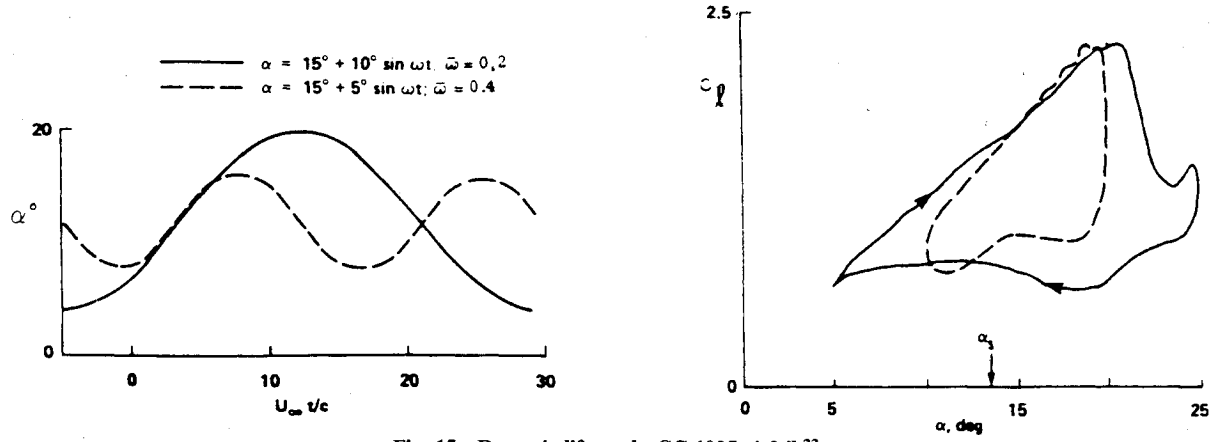

Fig. 15 Dynamic lift on the SC-1095 airfoil.[23]

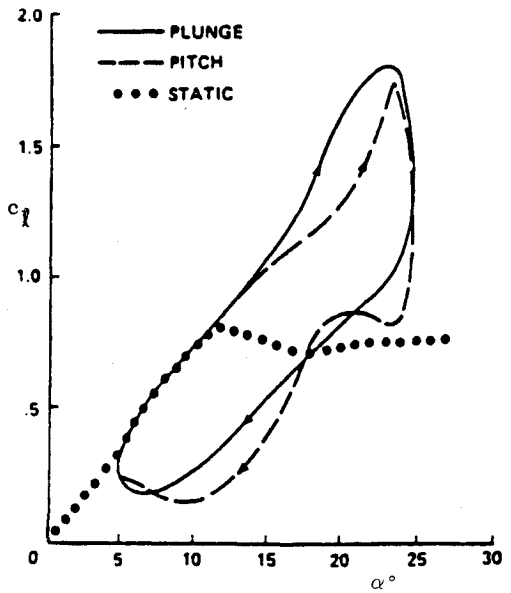

Fig. 16 Comparison of pitch and plunge data in deep stall.[25]

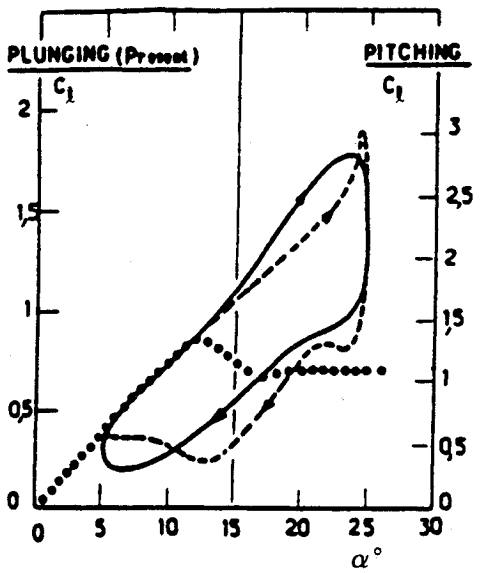

Fig. 17 Lift loops for pitching and plunging oscillations as presented in Ref. 26.

wall velocity (U_W) is constant around the circumference. It rotates the mean or time-average orientation of the flow separation, thereby producing (the stationary) Magnus lift. This usually occurs in the presence of an unsteady Kármán vortex shedding with associated oscillating flow separation.[16] $U_W/U_\infty > 2$ is required to suppress the Kármán vortex shedding. If the cylinder were to describe torsional oscillations at a frequency close to the Kármán vortex shedding frequency, the unsteady flow separation would, of course, be influenced. It is shown in Refs. 9 and 10 that the moving wall effect is only important in the boundary layer formation region near the stagnation point, becoming of negligible magnitude when $|\varphi| > 20$ deg. Consequently, the moving wall effect on flow separation (or transition) will not differ much for torsional and translational oscillations.

The moving wall effect on the unsteady flow separation will be largest when the cylinder oscillates at a frequency such that the moving wall effect on the boundary layer formation (at the stagnation point) has been convected down to the separation point at the time of flow separation. For other frequencies the flow separation will be affected by the much weaker moving wall effect existing away from the stagnation point. This "tuning" requirement is used in Ref. 10 to determine the frequency giving the maximum cylinder response to Kármán vortex shedding.

In addition to this self-excited type of response to the Kármán vortex shedding, there is the resonant-type response for frequencies near the Kármán vortex shedding frequency. The analysis in Ref. 10 provides the prediction shown in Fig. 10, which agrees well with the experimental results[1,2] shown earlier in Fig. 1. The analysis permits the response for zero external damping to be predicted[10] (Fig. 11). This would be the expected response in water, for example, where auxiliary damping usually is of negligible magnitude.

Dynamic Stall

When studying the characteristics of unsteady airfoil stall, it is instructive to start with the simple case of a ramp-wise change of angle of attack[18,19] (Fig. 12). The dynamic overshoot of the static stall angle has two components, $\Delta\alpha$ and $\Delta\alpha_s$. The first is purely a time lag effect, shifting the lift curve to the higher incidence $\alpha + \Delta\alpha$. The second component, $\Delta\alpha_s$, produces the experimentally observed overshoot, $\Delta c_{\ell\max} = c_{\ell\alpha}\,\Delta\alpha_s$, over the static lift maximum (at very high pitch-up rates there is also a significant contribution to $c_{\ell\max}$ from the "spilled" leading-edge vortex[20]). One contribution to the overshoot $\Delta\alpha_s$ comes from the beneficial accelerated flow effects on the developing boundary layer during the α-increasing phase of a pitching airfoil.[18] However, that this could not be the only contribution is evident from the experimental results[21] in Fig. 13. For example, in the case of the measured time average lift (it is itself above the static $c_{\ell\,\max}$, indicating that the instantaneous overshoot $\Delta c_{\ell\,\max}$ must have been very large), at $\alpha = 22$ deg, the oscillation amplitude $\Delta\theta \approx 6$ deg does not permit the airfoil to reach down below the static stall angle $\alpha_s \approx 10$ deg to experience the accelerated flow benefits, which can be realized only

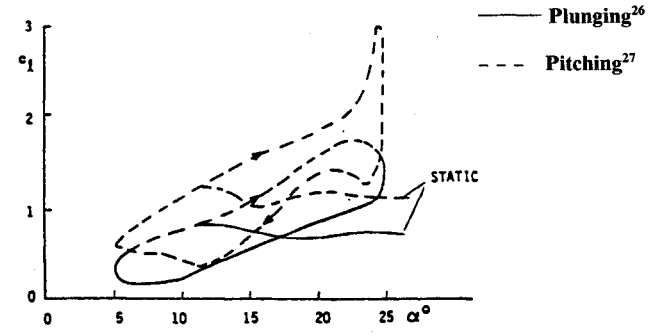

a) Original data

b) Zero-shifted data

Fig. 18 Lift loops plotted against a common lift scale.[28]

for initially attached flow. Another flow mechanism is clearly needed to explain the results in Fig. 13.

The other dynamic stall overshoot mechanism is the moving wall effect, the so-called "leading edge jet" effect illustrated in Fig. 14. As the leading edge moves upward during the "upstroke," the boundary layer is strengthened and stall delayed due to the large difference in tangential wall velocities at the stagnation point and the flow separation point on the top of the airfoil. Thus, through this wall jet-like effect the boundary layer has a fuller velocity profile and is, therefore, more difficult to separate. The "rolling leading edge" analogy in Fig. 14 was used[22] to illustrate the similarity to the classic moving wall effect, generating the Magnus lift shown in Figs. 1–6. In contrast to the accelerated flow effect, the "leading edge jet" effect is also present in the case of separated flow aft of the leading edge, permitting a gradual improvement of the boundary layer until it stays attached downstream of the leading edge. The analysis in Ref. 18 shows that accelerated flow and "leading edge jet" effects are proportional to the pitch-up rate and should, therefore, be simulated (aside from small deviations caused at high frequency and large amplitude by the nonlinear "spilled vortex" effect), if the maximum pitch-up rate $\dot{\alpha}c/U_\infty$ is simulated. The experimental results[23] in Fig. 15 confirm that this is the case ($|\dot{\alpha}c/U_\infty|$ is simulated if $\bar{\omega}\ \Delta\theta$ remains the same).

Pitching and Plunging Oscillations

It is clear from Fig. 14 that the moving wall effect, the so-called "leading edge jet" effect, will be different for a pitching and a plunging airfoil. Using Carta's nomenclature,[24] one can express the effective angle of attack as follows

$$\left.\begin{aligned} \alpha &= \alpha_o + \theta^* \\ \theta^* &= \bar{\alpha}\ \sin\omega t \\ \bar{\alpha} &= |\theta| = |\dot{z}|/U_\infty \end{aligned}\right\} \qquad (1)$$

where $\dot{z}/U_\infty$ is the "equivalent pitch."

Thus, when θ^* is increasing for the pitching airfoil, the "leading edge jet" effect is beneficial, whereas it is adverse for the plunging airfoil when θ^* is increasing. In spite of this fact, according to McCroskey, the dynamic stall analysis methods in

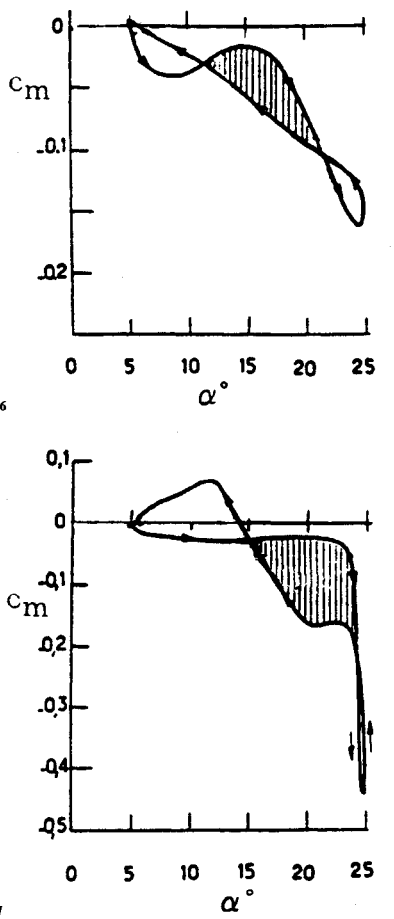

a) Plunging[26]

b) Pitching[27]

Fig. 19 Pitching moment loops for pitching and plunging oscillations.[26]

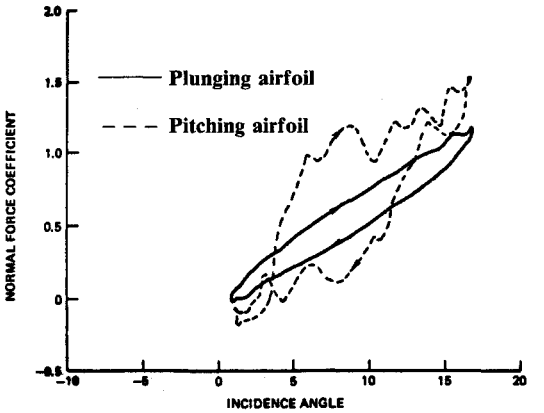

Fig. 20 Airfoil normal force characteristics in plunge and pitch.[24]

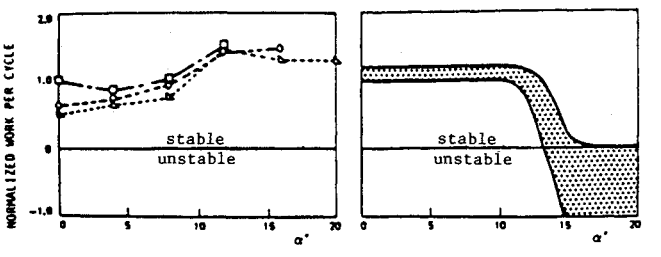

a) Rainey[30] b) Liiva et al[29]

Fig. 21 Normalized work per cycle for plunging oscillations.[24]

use (with one exception[18]) at the time of his review[25] all assumed that the similarity expressed by $\bar{\alpha}$ in Eq. (1) was valid. Figure 16 was used in Ref. 25 to illustrate the validity of Eq. (1). It was originally presented in Ref. 26 as shown in Fig. 17. The rationale behind the stretching of the ordinate scales was to make the dynamic $c_{\ell\,\max}$ the same, assuming that the measured difference was due to the large difference in Reynolds number between the pitching[27] and plunging[26] tests. Looking at the original "uncorrected" results (Fig. 18a), one finds that by simply zero-shifting the experimental curves one can get the static characteristics to agree. This also brings the initial θ^*-increasing portions of the loops to agree[28] (Fig. 18b). This is expected as the Reynolds number has little influence on these attached flow branches of the loops. In regard to the rest of the loops, moving wall effects are likely to dominate over deviations caused by the difference in Reynolds number between the two tests. The differences between the two loops in Fig. 18b can all be explained by the opposite moving wall effects, as is discussed at length in Ref. 28. The original pitching moment results (Fig. 19) give a more direct measurement of this difference, showing that the beneficial moving wall effects for the pitching airfoil delays stall to $\alpha \approx 24$ deg, whereas the adverse moving wall effects for the plunging airfoil causes stall to occur already at $\alpha \approx 16$ deg. Even in the case of a bluff-face configuration, such as a rectangular cross section, moving wall (or "leading edge jet") effects greatly influence the flow separation.[12] The difference between those effects for plunging and pitching oscillations have a profound effect on the coupling with Kármán vortex shedding.[12]

Anomalous Dynamic Stall Results

Carta's test[24] not only showed that Eq. (1) is not valid, it also produced the peculiar results shown in Figs. 20 and 21. Figure 20 reveals that the measured $c_{\ell\,\max}$ was larger for the plunging than for the pitching airfoil, contrary to the expected difference due to moving wall effects. Figure 21 adds to the confusion, showing that, instead of measuring the negative damping (represented by the normalized work per cycle) at stall obtained by Liiva,[29] Carta[24] obtained the same peculiar results as Rainey had obtained earlier,[30] i.e., the damping in the stall region was positive and even exceeded the attached flow damping. This "reversal" from the expected results has the same origin as the Magnus lift reversal discussed earlier (Figs. 1–6). That is, it is caused by the moving wall effects on boundary-layer transition with associated effects on the flow separation. Carta's hot film response data[24] (Fig. 22) show what is happening. Comparing the results for pitch and plunge one can see how the adverse moving wall effect $\dot{z}(t)$ promotes transition and causes the plunging airfoil to have a longer run of attached turbulent flow prior to stall. As a result, the flow stays attached past 7.5% chord, whereas flow separation occurs forward of 5% chord on the pitching airfoil, which has a shorter turbulent run before stall due to the opposite (transition-delaying) moving wall effect.

The effect on the plunging lift loop and associated damping of this coupling between airfoil motion and transition can be visualized using the static data[31] in Fig. 23. Instead of causing the discontinuous lift loss to be caught, e.g., for $Re = 0.66 \times 10^6$, the adverse "leading edge jet" effect on the plunging downstroke has an effect equivalent to increasing the Reynolds number, elevating the lift, for example, from that for $Re = 0.66 \times 10^6$ to $Re = 1.34 \times 10^6$. This causes the area enclosed by the plunging loop to be larger than that for attached flow, where this unsteady viscous flow effect is absent, resulting in the higher measured damping (represented by the normalized work per cycle) at stall shown in Fig. 21.

Three-Dimensional Flow

As a slender body of revolution is pitched through the angle-of-attack range from 0 to 90 deg, it experiences four distinct flow patterns that reflect the diminishing influence of the axial

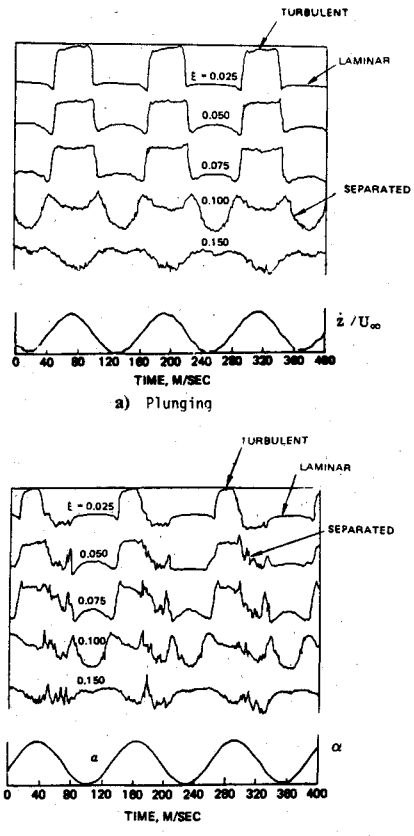

Fig. 22 Hot film response for pitching and plunging oscillations at $\alpha_o = 15$ deg, $\bar{\alpha} = 5$ deg, and $\bar{\omega} = 0.5$.[24]

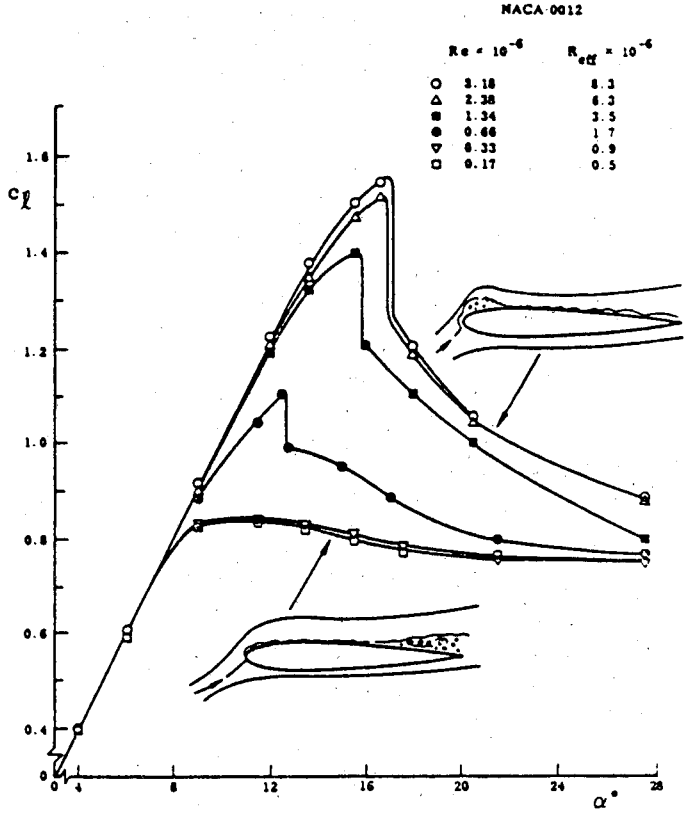

Fig. 23 Effect of Reynolds number on the lift characteristics of the NACA-0012 airfoil.[31]

flow component[32] (Fig. 24). At low angles of attack ($0 \leq \alpha < \alpha_{SV}$), the axial flow dominates, and the flow is attached, although crossflow effects will generate a thick viscous layer on the leeside. At intermediate angles of attack ($\alpha_{SV} \leq \alpha < \alpha_{AV}$), the crossflow separates and rolls up into a symmetric vortex pair. In the angle-of-attack range of steady asymmetric vortex shedding ($\alpha_{AV} \leq \alpha < \alpha_{UV}$), the axial flow component is still sufficiently large to produce steady vortices. However, the vortices become asymmetric, producing a side force and yawing moment even at zero sideslip. Finally, at very high angles of attack ($\alpha_{UV} \leq \alpha \leq 90$ deg), the axial flow component has less and less influence and the vortex shedding converts to the unsteady type, starting on the aft body and progressing forward to the nose with increasing angle of attack. That is, the leeside flow resembles the two-dimensional wake of a circular cylinder normal to the flow.

It is obvious from the discussion earlier of two-dimensional flow separation and associated vortex shedding that one can expect the moving wall effects to have a large influence also in the high-α, three-dimensional flow case illustrated in Fig. 24. Even a modest spin rate has a large effect on the developed side force[33,34] (Fig. 25). Test results for an ogive cylinder with a spinning nose tip[35] give a very vivid demonstration of how powerful the moving wall effects can be (Fig. 26). At $\alpha = 55$ deg, the crossflow conditions on the nose tip were apparently of the critical type shown in Figs. 4 and 6. Thus, even an infinitesimally small spin rate will cause reversal of the flow separation, and it is the direction rather than the rate of spin that determines the vortex-induced side force. For a more direct comparison of the three-dimensional flow case with the two-dimensional one in Figs. 1–6, please refer to Fig. 20 of Keener's flow visualization report.[36] The data in Fig. 26 show motion hysteresis effects similar to those measured by others. The critical condition shown in Fig. 26 has also been realized by an ogive-cylinder body in pitch-up motion,[37] with associated large effects on the unsteady aerodynamics.[38]

The experimental results[39] in Fig. 27 show that the three-dimensional moving wall effects can also be powerful for purely laminar flow conditions. The authors describe how only a slight push was needed to establish the coning motion in one direction or the other, regardless of the fact that the measured static yawing moment was biased in one direction due to nose microasymmetries.[32,40,41] The cone-cylinder body reached approximately equal steady-state coning rates in positive and negative rotation directions (Fig. 27). That is, the motion dominated over the static asymmetry, locking-in the vortex asymmetry in the direction of the body motion and driving it. In the case of a coning motion, the moving wall effects act as follows on the translating cross-section[42] (Fig. 28). The lateral motion of the circular cross section causes the flow separation to be delayed on the advancing side and promoted on the retreating side, the important moving wall effects being those generated near the flow stagnation point, as was discussed earlier. Thus, the motion produces a force that drives it until an equilibrium coning rate is reached, where the separation-induced driving moment is balanced by the drag-generated damping moment. This occurs also in the case of coning at $\alpha = 90$ deg, the flat-spin case[43] described in Ref. 44.

At critical flow conditions, the flat-spin motion controls completely the flow separation asymmetry, as is illustrated by the results[45] in Fig. 29. This is not too surprising, as in the free-to-spin case, which Fig. 29 simulates, the flat-spin rate reaches magnitudes $|\bar{\Omega}_{FS}/2| > 1$, i.e., at the tip the moving wall velocity exceeds the freestream velocity[43,44] (Fig. 30). Although

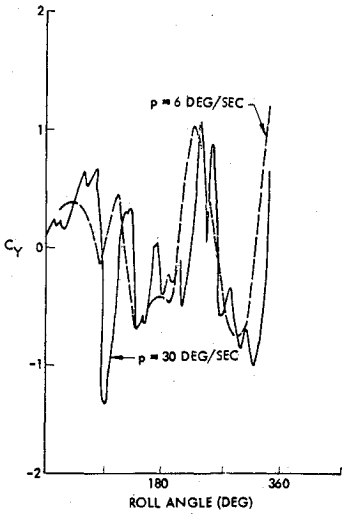

Fig. 25 Effect of roll angle and roll rate on vortex-induced side force on a cone-cylinder.[33]

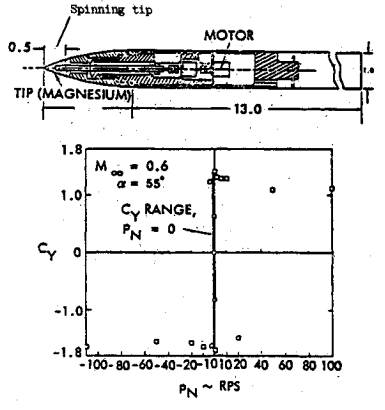

Fig. 26 Effect of spinning nose tip on vortex-induced side force.[35]

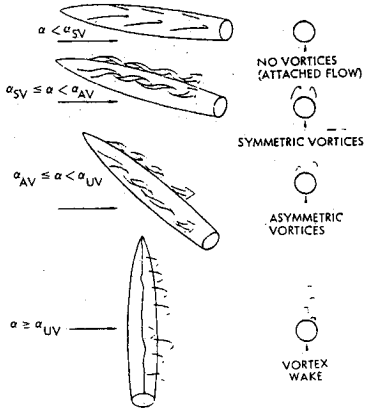

Fig. 24 Effect of angle of attack on leeside flowfield.

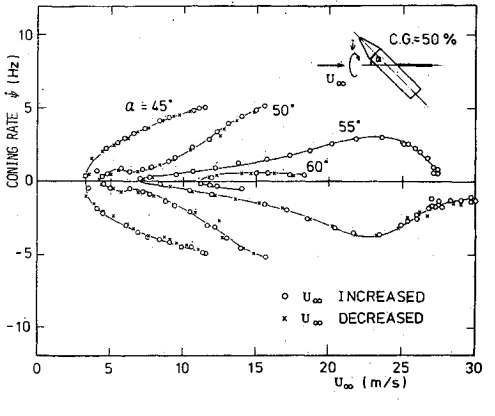

Fig. 27 Coning characteristics of a cone-cylinder.[39]

the flat spin is initiated by a subcritical/critical separation asymmetry with nonsymmetric spanwise distribution,[44–46] the very large moving wall effects cause a change to the critical/supercritical separation asymmetry illustrated in Fig. 31b before the final, limiting spin rate is reached (the open vector in Fig. 31 designates the sectional side force).

During the spin-up, the critical/critical flow separation asymmetry illustrated in Fig. 6b is established momentarily. However, the corresponding side force reversal does not last long enough to arrest the spin-up before the final separation asymmetry (shown in Fig. 31b) is established. Here the upstream moving wall effects on the retreating side have promoted transition to occur upstream of the flow separation, wiping out the laminar separation bubble. On the opposite, advancing side, the downstream moving wall effects delay transition, thereby prolonging the existence of the laminar separation bubble. This supercritical/critical separation asymmetry produces the maximum flat-spin rate (Fig. 30). The measured circumferential pressure distributions[45] in Fig. 29, obtained for close to the maximum flat-spin rate, show this critical type flow separation occurring at $\varphi \approx 140$ deg. At the limiting spin rate, the driving moment, generated by the flow separation asymmetry, is balanced by the damping moment, generated by the cross-sectional drag. Using two-dimensional cross-sectional characteristics one obtains[44]

$$\bar{\Omega}_{FS}/2 = (17/12)(\Delta c_\ell/c_d) \tag{2}$$

Applying a three-dimensional flow correction by use of the "aspect ratio" $1/d$ gives[44]

$$\bar{\Omega}_{FS}/2 = (17/12)(1 + 2D/1) \tag{3}$$

The maximum separation-induced side force Δc_ℓ is the vertical displacement between the two Magnus lift branches on both sides of the discontinuity in Figs. 2 and 3. Using the results in Fig. 4, one obtains the upper limit $\Delta c_\ell \approx 0.6$. The corresponding drag measurements are shown in Fig. 32, giving $c_d \approx 0.6$. Using these values, Eqs. (2) and (3) give the predictions[44] shown in Fig. 33. It can be seen that the experimental results[43] (Fig. 30) are bracketed by the predictions,[44] with Eq. (3) appearing to be the appropriate one to use for $1/d \leq 3$.

As in the case of the two-dimensional flow conditions,[12] noncircular cross sections also experience moving wall effects in three-dimensional flow, as is demonstrated by the measured forebody side force (forward of the rotation center) on a square cross-section body in flat spin[47] (Fig. 34). The angle β^*_{max} is the maximum motion-induced local flow incidence on the forebody (at the nose). As is discussed in Ref. 48, windward side flow reattachment in a static test of a square cross section will not occur until $\alpha > 10$ deg. This contrasts with the value $\beta^*_{max} \approx 1.25$ deg in Fig. 34, illustrating the power of the beneficial, downstream moving wall effects to cause early reattachment.

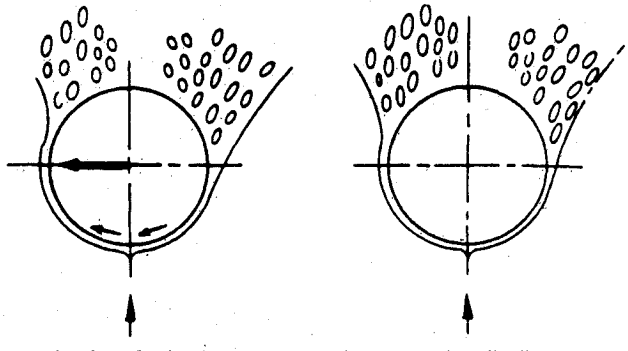

Fig. 28 Coning-induced translational moving wall effects.

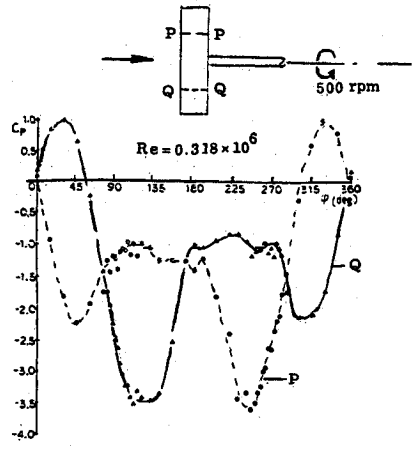

Fig. 29 Measured pressure distributions on a circular cylinder in flat spin.[45]

Moving Wall Effects on Transition

Experiments with a rotating circular cylinder, aligned axially with the flow at $\alpha = 0$, show that transition is promoted by body spin[49] (Fig. 35a). At angle of attack, the spin-induced promotion of transition is amplified greatly on the side where the spin-induced velocity opposes the α-induced crossflow (180 deg $< \varphi <$ 360 deg in Fig. 35b). Transition is delayed on the opposite side, where wall velocity and crossflow act in the same direction (0 $< \varphi <$ 180 deg in Fig. 35b). That is, the same type of upstream and downstream moving wall effects as in the case of two-dimensional flow (Figs. 1–6) exist also in this highly three-dimensional flow case, as is discussed more fully in Ref. 50. Tests with an ogive-cylinder body at $\alpha = 0$ and $\alpha = 6$ deg demonstrate how powerful the spin-induced transition-promotion can be[51] (Fig. 36). At $\alpha = 6$ deg, Reynolds number and upstream wall velocity need only be a fraction of what they are at $\alpha = 0$ to cause the earliest local transition to occur at the same axial location.

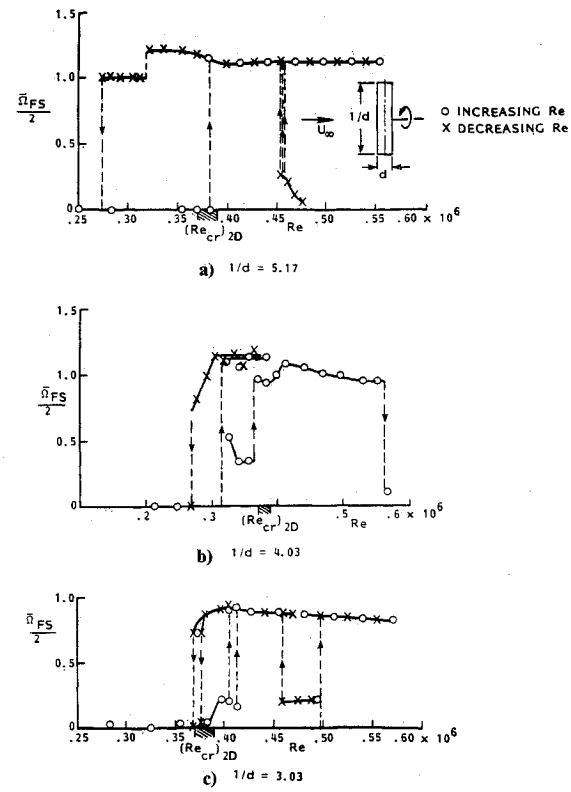

Fig. 30 Effect of "aspect ratio" $1/d$ on flat-spin rate of a circular cylinder.

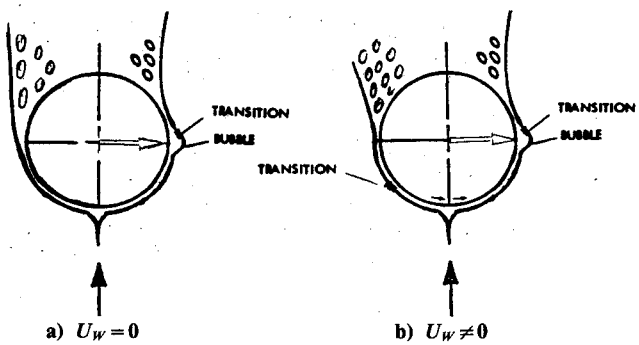

Fig. 31 Moving wall effects on a translating circular cross section at critical flow conditions.

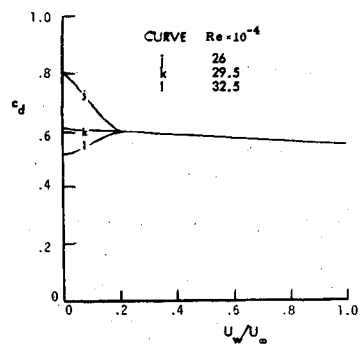

Fig. 32 Moving wall effects on cylinder drag in the critical flow region.[2]

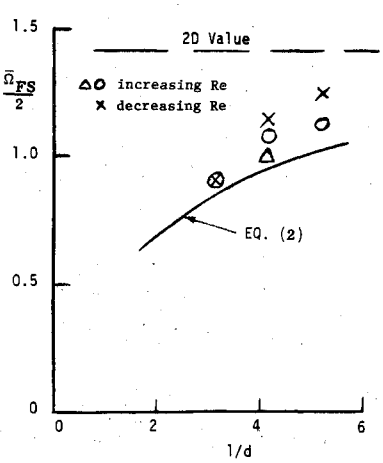

Fig. 33 Comparison of predicted and measured maximum flat-spin rate.[44]

The moving wall effects for spinning and coning bodies are somewhat similar (Fig. 37). Instead of being constant, as in the spinning case, on the coning body the moving wall velocity varies around the periphery. The maximum wall velocity, $U_{W\max}$, occurs on top and bottom meridians, with only the latter being of importance. The thick leeward side boundary layer is completely dominated by viscous crossflow effects.[50] At supersonic speeds, the transition bulge will generate a side force that drives the coning motion. It is discussed in Ref. 50 how this explains the behavior observed on slender reentry vehicles,[52] where the motion changes from the precessing planar to the coning type when transition starts occurring on the windward side, where the full potential of the moving wall effects can be realized.

Moving Wall Effects on Transition and Separation

At higher angles of attack, $\alpha > 30$ deg, the moving wall effects on transition are very much the same as in two-dimen-

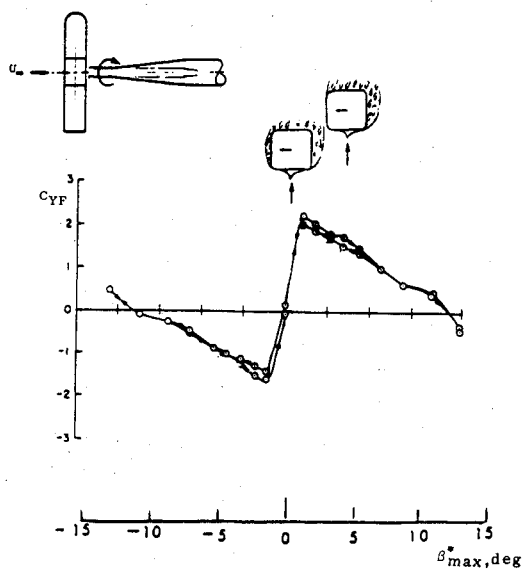

Fig. 34 Subcritical side force characteristics of a square cross section forebody in flat spin.[47]

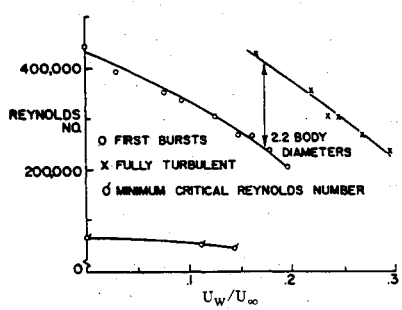

a) $\alpha = 0$

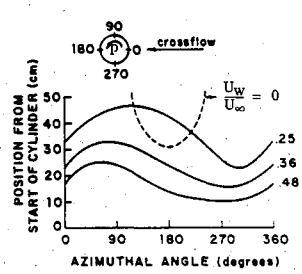

b) $\alpha = 3$ deg

Fig. 35 Effect of spin rate on low-speed transition on a circular cylinder shell.[49]

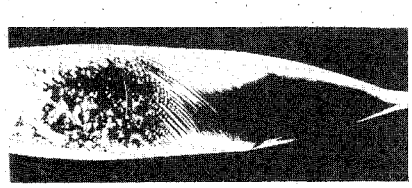

a) $\alpha = 0$, $U_W/U_\infty = 0.825$, $Re_1 = 0.814 \times 10^6$

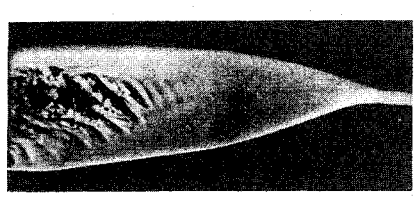

b) $\alpha = 6$ deg, $U_w/U_\infty = 0.169$, $Re_1 = 0.315 \times 10^6$

Fig. 36 Smoke flow visualization of transition on a spinning ogive-cylinder at low speeds.[51]

sional flow.[32,40,41] This provides a simple explanation[53] of the wing rock observed for a rather innocent-looking wing-body configuration[54] (Fig. 38). The Reynolds number of the test, $Re \approx 0.3 \times 10^6$, is in the critical region (see Fig. 4), providing the following scenario[53] (Fig. 39). At $t = t_1$ the upstream moving wall effect causes boundary layer transition to occur in the forebody crossflow before separation occurs. This changes the portside flow separation from the subcritical towards the supercritical type. In absence of time lag effects, the vortex geometry sketched at $t = t_1$, would result. Due to time lag effects, similar to those present in the case of slender wing rock,[55] this vortex geometry (only the lower vortex is shown as only it will induce significant loads on the wing-body) is not realized until $t = t_1 + \Delta t$. At $t = t_3$, when the roll rate reaches its maximum in the opposite direction, another forebody switch of separation asymmetry occurs. Because of the time lag effect,[55] the vortex geometry at the now horizontal wing has not changed, but will be of the type shown for $t = t_1 + \Delta t$, in agreement with the vortex behavior observed through smoke flow visualization.[54]

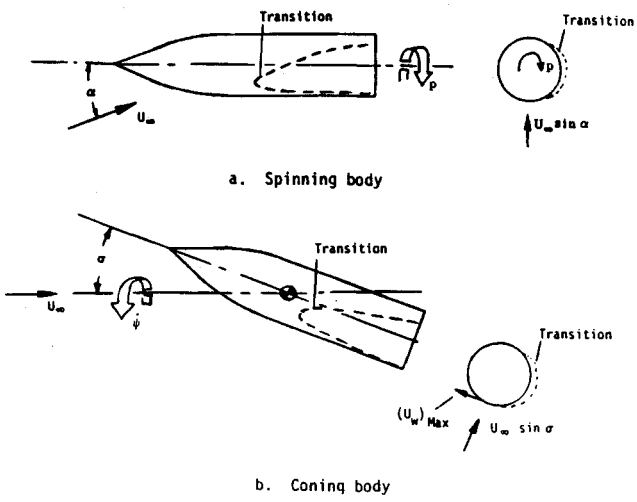

Fig. 37 Conceptual moving wall effects on transition for a slender body in spinning or coning motion.[50]

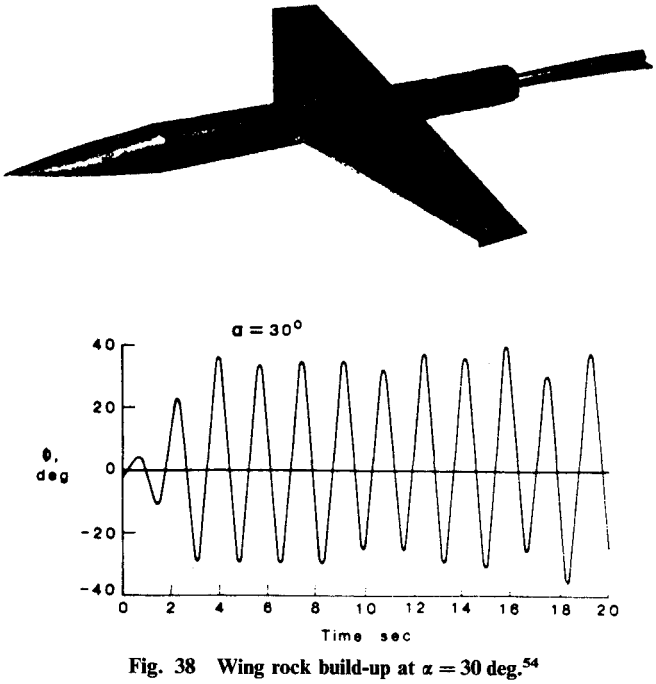

Fig. 38 Wing rock build-up at $\alpha = 30$ deg.[54]

Similar moving wall effects on transition can explain the oscillatory coning behavior observed experimentally for a cone-cylinder body flying backwards[39] (Fig. 40). The mirror symmetry of the limiting coning rates is very similar to that obtained for the regular nose-forward orientation (Fig. 27). However, in this case no exterior push was needed to change the coning direction. The measured acceleration and coning rates are shown in Fig. 41. It can be seen that, when a certain limiting coning rate is reached, the acceleration suddenly switches sign. The fluid mechanical process can be described as follows,[42] with the aid of the inserted flow sketches. Initially, flow asymmetry or minute surface irregularities set the separation asymmetry, initiating the coning motion. The coning-induced moving wall effects delay the laminar separation on the advancing side, resulting in positive coning velocity and spin acceleration ($\dot{\psi}$ and $\ddot{\psi} > 0$). However, the adverse upstream moving wall effect eventually causes boundary layer transition on the retreating side, the effect being very similar to the one observed for the rotating cylinder[2] (Fig. 2). This reverses the separation asymmetry and the coning motion starts to decelerate ($\dot{\psi} > 0$, $\ddot{\psi} < 0$). Eventually, this results in accelerated coning in the opposite direction ($\dot{\psi}$ and $\ddot{\psi} < 0$). The coning reversal moves transition back into the wake on the new advancing side, and asymmetric laminar separation is reestablished. Eventually, transition occurs on the retreating side to cause critical/subcritical separation asymmetry, reversing the vortex asymmetry and decelerating the coning motion ($\dot{\psi} < 0$,

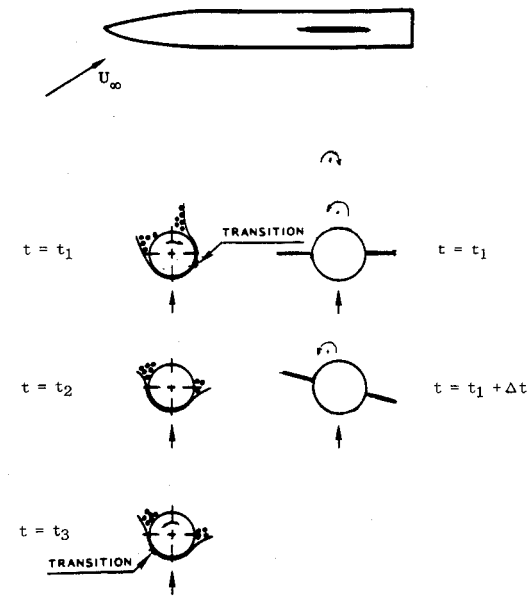

Fig. 39 Conceptual flow mechanism for wing-body rock.[53]

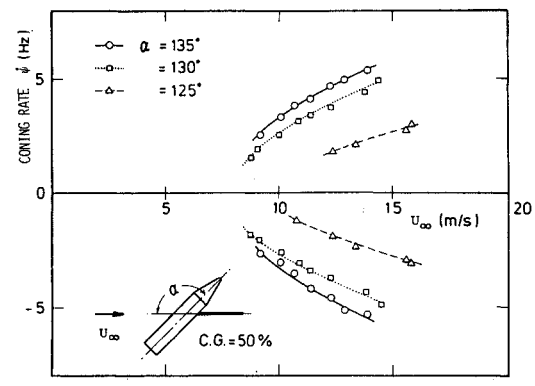

Fig. 40 Coning rates of cone-cylinder at $\alpha > 90$ deg.[39]

$\dot{\psi} > 0$). The process continually repeats itself, resulting in a self-reversing coning motion.

Apparently, the test Reynolds number was not high enough to establish the necessary high laminar flow conditions on the conic nose[39] (Fig. 27). One can see, however, how with increasing Reynolds number the successive establishment on the nose of the flow conditions illustrated in Figs. 2, 4, and 3, respectively, is possible, generating variations of the self-reversing coning conditions illustrated in Figs. 39 and 40. Thus, for an aircraft or missile in free flight, one can foresee a strong coupling between wing rock and coning. As the vortex strength (and flow separation extent) will depend strongly upon the angle of attack, one can indeed expect a strong coupling to exist between the three angular degrees of freedom, as has been pointed out by Orlik-Rückemann.[56]

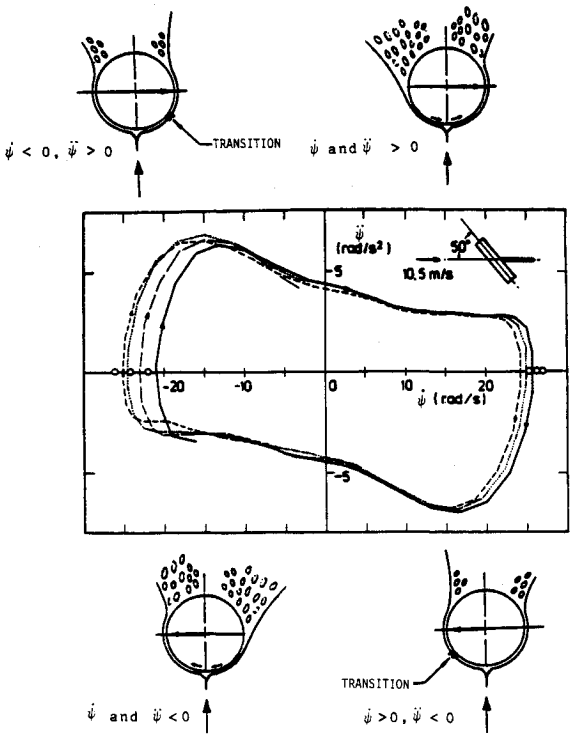

Fig. 41 Acceleration-rate time history for a flat-faced circular cylinder coning at $\alpha = 50$ deg.[32]

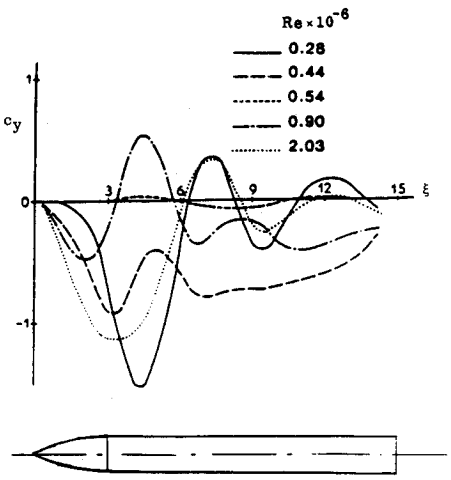

Fig. 42 Side force distribution at $\alpha = 50$ deg on an ogive-cylinder through the critical Reynolds number range.[57]

In view of the strong interplay between Reynolds number and moving wall effects just demonstrated, Champigny's experimental results[57] (Fig. 42) give cause for the concerns expressed in Refs. 32, 38, and 42 that in full scale flight a vehicle maneuver could lock-in the single cell flow separation asymmetry along the full length of a missile or aircraft forebody.

Moving Separation Point Effect: An Apparent Moving Wall Effect

In unsteady flow separation, the upstream movement of the separation point has an effect equivalent to that of a downstream moving wall, as has been pointed out by Moore.[58] In Ref. 22, the experimental results for a rotating circular cylinder, obtained by Moore's associates Brady and Ludwig,[59] are used to estimate the effect of the moving separation point on dynamic airfoil stall (Fig. 43). When the separation point starts to move upstream, the boundary layer, starting to separate, "sees" a downstream moving wall (Fig. 43b), and flow separation is delayed. The corresponding phase lag for the airfoil is

$$\Delta\phi_{sp} = \xi_{sp}\bar{\omega} \tag{4}$$

where

$$\xi_{sp} = \partial\xi_s/\partial(U_W/U_\infty) \tag{5}$$

Using the rotating cylinder data obtained by Brady and Ludwig (Fig. 43a), who used a shroud over the cylinder top to impose an airfoil-like pressure distribution, one obtains the value $\xi_{sp} = 3.0$ for laminar flow, and $\xi_{sp} = 0.75$ for turbulent flow, with $\xi_s = x_s/c$ assuming $c \approx r$.

The shedding or "spilling",[20] of the leading edge stall vortex is delayed by this phase lag $\Delta\phi_{sp}$. When one adds the phase lag occurring before the spilled vortex has traveled across the airfoil,[20] one can predict the interesting phenomenon of lift stall inhibition observed in dynamic experiments.[60]

When the forward movement of the separation point stops, the vortex shedding process starts. According to Carta's measurements for a NACA-0012 airfoil,[61] the vortex shedding has an initial growing phase, during which it moves downstream very slowly. The corresponding phase lag is

$$\Delta\phi_{vg} = \xi_{vg}\bar{\omega} \tag{6}$$

where

$$\xi_{vg} \approx 0.90$$

In view of the overwhelming evidence of the power of the moving wall effects, it is reassuring to find that theoreticians are now beginning to recognize this phenomenon.[62,63]

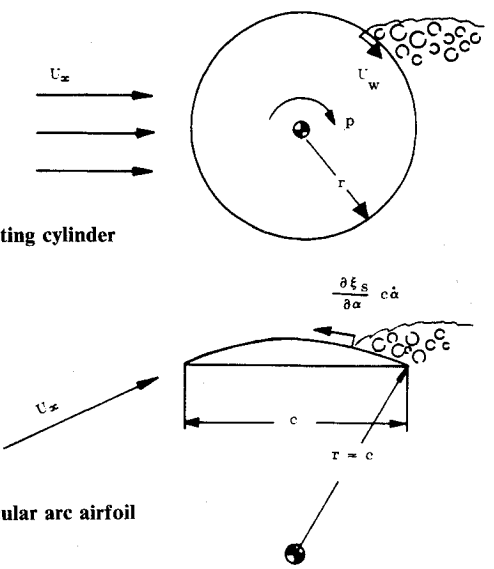

Fig. 43 Moving separation point—moving wall analogy.[22]

Conclusions

A selective review of the existing experimental evidence of moving wall effects on unsteady aerodynamic characteristics leads to the following conclusions:

1) The moving wall effect is present both in two-dimensional and three-dimensional flows.

2) Its effect on the separation of purely laminar or turbulent boundary layers is rather straightforward.

3) Its effect on boundary layer transition can influence the unsteady aerodynamics significantly even in absence of flow separation.

4) When the moving wall effect influences flow separation via the boundary layer transition mechanism, not only is the total moving wall effect much more complicated, but, as a rule, it also has a much larger influence on the unsteady aerodynamics than in the case of purely laminar or turbulent boundary layer separation.

5) In most full scale flight cases, one will have to deal with this more complex form of the moving wall effect.

References

[1]Magnus, G., "On the Deflection of a Projectile," *Abhandlung der Akademie der Wissenschaften*, Berlin, Germany, 1852.

[2]Swanson, W. M., "The Magnus Effect: A Summary of Investigations to Date," *Journal of Basic Engineering*, Vol. 83, Sept. 1961, pp. 461–470.

[3]Ericsson, L. E., "Kármán Vortex Shedding and the Effect of Body Motion," *AIAA Journal*, Vol. 18, Aug. 1980, pp. 935–944.

[4]Achenbach, E., "Influence of Surface Roughness on the Cross-Flow Around a Circular Cylinder," *Journal of Fluid Mechanics*, Vol. 46, Pt. 2, 1971, pp. 321–335.

[5]Furguson, N., "The Measurement of Wake and Surface Effects in the Subcritical Flow Past a Circular Cylinder at Rest and in Vortex-Excited Oscillations," M.A. Sc.Thesis, Univ. of British Columbia, Vancouver, Sept. 1965.

[6]Furguson, N. and Parkinson, G. V., "Surface and Wake Phenomena of the Vortex-Exited Oscillation of a Circular Cylinder," *Journal of Engineering for Industry*, Vol. 89, No. 3, Nov. 1967, pp. 831–838.

[7]Ericsson, L. E., "Unsteady Aerodynamics of Separating and Reattaching Flows on Bodies of Revolution," *Recent Research on Unsteady Boundary Layers*, Vol. 1, International Union of Theoretical and Applied Mechanics Symposium, 1971, pp. 481–512.

[8]Ogava, A. and Nakagawa, K., "Stability of the Vortex Sheet in the Wake of Stationary and Vibrating Cylinders," *Transactions of the Japan Society of Aerospace Science*, Vol. 20, Feb. 1978, pp. 167–176.

[9]Ericsson, L. E., "Maximum Crossflow Response of a Circular Cylinder, a Non-Resonant Flow Phenomenon," AIAA Paper 84-0422, Jan. 1984.

[10]Ericsson, L. E., "Circular Cylinder Response to Kármán Vortex Shedding," AIAA Paper 86-0999-CP, May 1986.

[11]Ericsson, L. E., "Limit Amplitude of Galloping Bluff Cylinders," *AIAA Journal*, Vol. 22, April 1984, pp. 493–497.

[12]Ericsson, L. E., "Kármán Vortex Shedding: Friend or Foe of the Structural Dynamicist?," *Journal of Aircraft*, Vol. 23, Aug. 1986, pp. 621–628.

[13]Morris, A. W., "A Review on Vortex Sheets, Periodic Wakes, and Induced Vibration Phenomena," *Journal of Basic Engineering*, Vol. 86, June 1964, pp. 185–196.

[14]Bublitz, P., "The Periodic Normal Force on a Circular Cylinder in Cross Flow—An Unsteady Magnus Effect," *Z. Flugwiss. Weltraumforsch*, Vol. 7, Heft 4, 1983, pp. 253–262.

[15]Ericsson, L. E. and Reding, J. P., "Unsteady Flow Concepts for Dynamic Stall Analysis," *Journal of Aircraft*, Vol. 21, Aug. 1984, pp. 601–606.

[16]Dwyer, H. A. and McCroskey, W. J., "Oscillating Flow Over a Cylinder at Large Reynolds Number," *Journal of Fluid Mechanics*, Vol. 61, Pt. 4, 1973, pp. 753–767.

[17]Diaz, F., Gavalda, J., Kawall, J. G., Keller, J. F., and Giralt, F., "Vortex Shedding from a Spinning Cylinder," *Physics of Fluids*, Vol. 26, Dec. 1983, pp. 3454–3460.

[18]Ericsson, L. E. and Reding, J. P., "Dynamic Stall Analysis in Light of Recent Numerical and Experimental Results," *Journal of Aircraft*, Vol. 13, April 1976, pp. 248–255.

[19]Harper, P. W. and Flanigan, R. E., "The Effect of Rate of Change of Angle of Attack on Maximum Lift of a Small Model," NACA TN 206, 1949.

[20]Ericsson, L. E. and Reding, J. P., "Dynamic Stall at High Frequency and Large Amplitude," *Journal of Aircraft*, Vol. 17, March 1980, pp. 136–142.

[21]Halfman, R. L., Johnson, H. C., and Haley, S. M., "Evaluation of High-Angle-of-Attack Aerodynamic Derivative Data and Stall Flutter Prediction Techniques," NACA TN 2533, 1951.

[22]Ericsson, L. E. and Reding, J. P., "Analytic Prediction of Dynamic Stall Characteristics," AIAA Paper 76-682, June 1972.

[23]McCroskey, W. J., McAlister, K. W., Carr, L. W., Pucci, S. L., Lambert, O., and Indergrand, R. F., "Dynamic Stall on Advanced Airfoil Sections," *Journal of the American Helicopter Society*, Vol. 13, July 1981, pp. 40–50.

[24]Carta, F. O., "A Comparison of the Pitching and Plunging Response of an Oscillating Airfoil," NASA CR-3172, Oct. 1979.

[25]McCroskey, W. J., "The Phenomenon of Dynamic Stall," NASA TM 81264 and Paper 2, von Kármán Institute Lecture Series 1981-4, March 1981.

[26]Maresca, C. A., Favier, D. J., and Rebont, J. M., "Unsteady Aerodynamics of an Airfoil at High Angle of Incidence Performing Various Linear Oscillations in a Uniform Stream," *Journal of the American Helicopter Society*, Vol. 3, April 1981, pp. 40–45.

[27]Carr, L. W., McAlister, K. W., and McCroskey, W. J., "Analysis of Development of Dynamic Stall Based on Oscillating Airfoil Experiments," NASA TN D-8382, 1977.

[28]Ericsson, L. E. and Reding, J. P., "The Difference Between the Effects of Pitch and Plunge on Dynamic Airfoil Stall," Paper 8, 9th European Rotorcraft Forum, Stresa, Italy, Sept. 1983.

[29]Liiva, J., "Unsteady Aerodynamic and Stall Effects on Helicopter Rotor Blade Airfoil Sections," *Journal of Aircraft*, Vol. 6, Jan.–Feb. 1969, pp. 46–51.

[30]Rainey, A. G., "Measurement of Aerodynamic Forces for Various Mean Angles of Attack on an Airfoil Oscillating in Bending with Emphasis on Damping in Stall," NACA Rept. 1305, 1957.

[31]Jacobs, E. N. and Sherman, A., "Airfoil Section Characteristics as Affected by Variations in the Reynolds Number," NACA Tech. Rept. 586, 1973.

[32]Ericsson, L. E. and Reding, J. P., "Asymmetric Vortex Shedding from Bodies of Revolution," Chap. VII, *Tactical Missile Aerodynamics*, Vol. 104, Progress Astronautics and Aeronautics Series, AIAA, 1986, pp. 243–296.

[33]Atraghji, E. G., "The Influence of Mach Number, Semi-Nose Angle and Roll Rate on the Development of the Forces and Moments Over a Series of Long Slender Bodies of Revolution at Incidence," National Research Council, Ottawa, Canada, National Aeronautical Establishment Data Rept. 5 × 5/0020, 1967.

[34]Kruse, R. L., "Influence of Spin Rate on Side Force of an Axisymmetric Body," *AIAA Journal*, Vol. 12, July 1974, pp. 1003–1005.

[35]Fidler, J. E., "Active Control of Asymmetric Vortex Effects," *Journal of Aircraft*, Vol. 18, April 1981, pp. 267–272.

[36]Keener, E. R., "Flow-Separation Patterns on Symmetric Forebodies," NASA TM 86016, Jan. 1986.

[37]Smith, L. H., "Aerodynamic Characteristics of an Axisymmetric Body Undergoing a Uniform Pitching Motion," Ph.D. Dissertation, Naval Post-Graduate School, Monterey, CA, Dec. 1974.

[38]Ericsson, L. E. and Reding, J. P., "Steady and Unsteady Vortex-Induced Asymmetric Loads on Slender Vehicles," *Journal of Spacecraft and Rockets*, Vol. 18, March–April 1981, pp. 97–109.

[39]Yoshinaga, T., Tate, A., and Inoue, K., "Coning Motion of Slender Bodies at High Angles of Attack in Low Speed Flow," AIAA Paper 81-1899, Aug. 1981.

[40]Ericsson, L. E. and Reding, J. P., "Review of Vortex-Induced Asymmetric Loads—Part I," *Zeitschrift für Flugwissenschaften und Wetraumfahrt*, Heft 3, 1981, pp. 162–174.

[41]Ericsson, L. E. and Reding, J. P., "Review of Vortex-Induced Asymmetric Loads—Part II," *Zeitschrift für Flugwissenschaften und Wetraumfahrt*, Heft 6, 1982, pp. 349–366.

[42]Ericsson, L. E. and Reding, J. P., "Dynamics of Forebody Flow Separation and Associated Vortices," *Journal of Aircraft*, Vol. 22, April 1985, pp. 329–335.

[43]Yoshinaga, T. and Tate, A., "Flat Spin of Slender Bodies Near the Critical Reynolds Number Region," to be published, private communication, Dec. 1985.

[44]Ericsson, L. E., "Flat Spin of Axisymmetric Bodies in the Critical Re-Region," *Journal of Spacecraft and Rockets*, Vol. 24, Nov.–Dec. 1987, pp. 532–538.

[45]Kubota, H., Irai, I., and Matsuzaka, M., "Wind Tunnel Investigations for the Flat Spin of Slender Bodies at High Angles of Attack," *Journal of Spacecraft and Rockets*, Vol. 20, March–April 1983, pp. 108–114.

[46]Ericsson, L. E., "Flat Spin of Bodies with Circular Cross Section," AIAA Paper 83-2147, Aug. 1983.
[47]Malcolm, G. N. and Clarkson, M. H., "Wind Tunnel Testing with a Rotary-Balance Apparatus to Simulate Aircraft Spin Motions," *Proceedings of the AIAA 9th Aerodynamic Testing Conference*, 1976, pp. 143–146.
[48]Ericsson, L. E., "Aerodynamic Characteristics of Noncircular Bodies in Flat Spin and Coning Motions," *Journal of Aircraft*, Vol. 22, May 1985, pp. 387–392.
[49]Morton, J. B., Jacobson, I. D., and Sounders, S., "Experimental Investigation of the Boundary Layer on a Rotating Cylinder," *AIAA Journal*, Vol. 14, Oct. 1976, pp. 1458–1463.
[50]Ericsson, L. E., "Coupling Between Vehicle Motion and Slender Cone Transition," *AIAA Journal*, Vol. 25, Sept. 1987, pp. 1194–1199.
[51]Kegelman, J. T., Nelson, R. C., and Mueller, T. J., "Boundary Layer and Side Force Characteristics of a Spinning Axisymmetric Body," AIAA Paper 80-1584, Aug. 1980.
[52]Chrusciel, G. T., "Analysis of R/V Behavior During Boundary Layer Transition," AIAA Paper 74-109, Jan. 1974.
[53]Ericsson, L. E., "Wing Rock Generated by Forebody Vortices," AIAA Paper 87-0268, Jan. 1987.
[54]Brandon, J. M. and Nguyen, L. T., "Experimental Study of Effects of Forebody Geometry on High Angle of Attack Static and Dynamic Stability," AIAA Paper 86-0331, Jan. 1986.
[55]Ericsson, L. E., "The Fluid Mechanics of Slender Wing Rock," *Journal of Aircraft*, Vol. 21, May 1984, pp. 322–328.
[56]Orlik-Rückemann, K. J., "Aerodynamic Aspects of Aircraft Dynamics at High Angles of Attack," *Journal of Aircraft*, Vol. 20, Sept. 1983, pp. 737–752.
[57]Champigny, P., "Reynolds Number Effect on the Aerodynamic Characteristics of an Ogive-Cylinder at High Angles of Attack," AIAA Paper 84-2176, Aug. 1984.
[58]Moore, F. K., "On the Separation of the Unsteady Laminar Boundary Layer," International Union of Theoretical and Applied Mechanics Symposium on Boundary Layer Research, 1957, pp. 296–311.
[59]Brady, W. G. and Ludwig, G. R., "Research on Unsteady Stall of Axial Flow Compressors," Rept. AM-1762-S-4, Cornell Aerospace Lab., Buffalo, NY, Nov. 1963.
[60]McCroskey, W. J. and Philippe, J. J., "Unsteady Viscous Flow on Oscillating Airfoils," *AIAA Journal*, Vol. 13, Jan. 1975, pp. 71–79.
[61]Carta, F. O., "Analysis of Oscillatory Pressure Data Including Dynamic Stall Effects," NASA CR-2394, May 1974.
[62]Laschka, B., "Unsteady Flows—Fundamentals and Applications," Paper 1, AGARD-CP-386, Nov. 1985.
[63]Tobak, M. and Chapman, G. T., "Nonlinear Problems in Flight Dynamics Involving Aerodynamic Bifurcation," Paper 25, AGARD-CP-386, Nov. 1985.